Neal P. Dillon[1]
Department of Mechanical Engineering,
Vanderbilt University,
2301 Vanderbilt Place,
PMB 351592,
Nashville, TN 37235
e-mail: neal.p.dillon@vanderbilt.edu

Ramya Balachandran
Department of Otolaryngology,
Vanderbilt University Medical Center,
1215 21st Avenue South,
MCE 10450,
Nashville, TN 37232
e-mail: ramya.balachandran@vanderbilt.edu

J. Michael Fitzpatrick
Department of Electrical Engineering and
Computer Science,
Vanderbilt University,
2301 Vanderbilt Place,
PMB 351679,
Nashville, TN 37235
e-mail: j.michael.fitzpatrick@vanderbilt.edu

Michael A. Siebold
Department of Electrical Engineering and
Computer Science,
Vanderbilt University,
2301 Vanderbilt Place,
PMB 351679,
Nashville, TN 37235
e-mail: michael.a.siebold@vanderbilt.edu

Robert F. Labadie
Department of Otolaryngology,
Vanderbilt University Medical Center,
1215 21st Avenue South,
MCE 10450,
Nashville, TN 37232
e-mail: robert.labadie@vanderbilt.edu

George B. Wanna
Department of Otolaryngology,
Vanderbilt University Medical Center,
1215 21st Avenue South,
MCE 10450,
Nashville, TN 37232
e-mail: george.wanna@vanderbilt.edu

Thomas J. Withrow
Department of Mechanical Engineering,
Vanderbilt University,
2301 Vanderbilt Place,
PMB 351592,
Nashville, TN 37235
e-mail: thomas.j.withrow@vanderbilt.edu

Robert J. Webster, III
Department of Mechanical Engineering,
Vanderbilt University,
2301 Vanderbilt Place,
PMB 351592,
Nashville, TN 37235
e-mail: robert.webster@vanderbilt.edu

A Compact, Bone-Attached Robot for Mastoidectomy

Otologic surgery often involves a mastoidectomy, which is the removal of a portion of the mastoid region of the temporal bone, to safely access the middle and inner ear. The surgery is challenging because many critical structures are embedded within the bone, making them difficult to see and requiring a high level of accuracy with the surgical dissection instrument, a high-speed drill. We propose to automate the mastoidectomy portion of the surgery using a compact, bone-attached robot. The system described in this paper is a milling robot with four degrees-of-freedom (DOF) that is fixed to the patient during surgery using a rigid positioning frame screwed into the surface of the bone. The target volume to be removed is manually identified by the surgeon pre-operatively in a computed tomography (CT) scan and converted to a milling path for the robot. The surgeon attaches the robot to the patient in the operating room and monitors the procedure. Several design considerations are discussed in the paper as well as the proposed surgical workflow. The mean targeting error of the system in free space was measured to be 0.5 mm or less at vital structures. Four mastoidectomies were then performed in cadaveric temporal bones, and the error at the edges of the target volume was measured by registering a postoperative computed tomography (CT) to the pre-operative CT. The mean error along the border of the milled cavity was 0.38 mm, and all critical anatomical structures were preserved.
[DOI: 10.1115/1.4030083]

1 Introduction

Mastoidectomy is a common procedure in otologic surgery that consists of removal of all or part of the mastoid portion of the temporal bone with a high-speed surgical drill. The procedure can be performed on its own to treat diseases and infections such as mastoiditis and cholesteatoma, or it can be performed as a component of other surgeries such as a facial recess approach for cochlear implantation (CI) or translabyrinthine approach for acoustic neuroma removal. During a facial recess approach for CI, a mastoidectomy is followed by opening the region just anterior to the facial nerve to allow access to the cochlea. During a translabyrinthine approach for acoustic neuroma (a.k.a. vestibular schwannoma) removal, a mastoidectomy is followed by a labyrinthectomy in which deeper dissection into the temporal bone removes a portion of the inner ear to allow access to the skull base, specifically the internal auditory canal (IAC) where the tumor is located.

Many critical anatomical structures are embedded within the bone of the mastoid (Fig. 1) including the facial nerve, which controls motion of the face, large blood vessels such as the carotid artery and intracranial continuation of the jugular vein, and the tegmen, which is the boundary between the mastoid and the brain. Because injury to these vital structures can lead to morbidity, surgeons manually identify these structures using visual and tactile feedback and then remove bone as needed around them. This identification is challenging and makes ear surgery, and mastoidectomy, in particular, well-suited for image-guided robotic assistance. We hypothesize that a robotic system guided by preoperative images could be used to remove bone, while preserving appropriate safety margins around the critical structures within the bone. By automating the bulk removal of bone using image-guidance, such a system would allow surgeons to focus on the more delicate portions of the surgery (e.g., inserting the electrode array for CI, or removing the acoustic neuroma from the brainstem) and could potentially save time in the operating room, thereby reducing the cost of caring for each patient.

Robotic bone milling has been a topic of research and commercial development for over 20 years [1–3] with most work focusing on orthopedic procedures such as joint arthroplasty and resurfacing. Several of these systems have been successfully commercialized and are currently used clinically (e.g., RIO System by MAKO Surgical Corp., Ft. Lauderdale, FL; ROBODOC Surgical System by Curexo Technology Corp., Fremont, CA; and CASPAR by URS Ortho GMBH & Co. KG, Rastatt, Germany). Bone milling is a task well-suited for robotic assistance, and because of the similarities to computer-numeric-control (CNC) machining, was one of the first surgical procedures to employ a robot. The rigidity of bone allows for the entire procedure to be planned preoperatively since deformity of bone geometry during surgery is minimal. Robotic milling of the temporal bone in ear surgery is a logical extension of previous robotic orthopedic procedures. However, ear surgery presents additional challenges not encountered in orthopedic procedures primarily due to the presence of relatively small and complex anatomy in and around the target regions. As such, the task requires submillimetric accuracy [4].

Several research groups have investigated robotic mastoidectomy [5–8] and have successfully demonstrated such in the laboratory. Like their orthopedic predecessors, these systems use large, free-standing robots. These robots take up significant space in the operating room and typically provide a workspace that is larger than the necessary workspace for otologic surgery. Additionally, free-standing robots require an alignment between the robot's coordinate system and the patient's anatomy throughout the procedure. The alignment is typically performed using an optical tracking system that continuously monitors the robot and the patient. These systems provide excellent image guidance for many procedures; however, the error associated with a tracking system, compounded with errors in other components of the system, makes it difficult to meet the submillimetric accuracy requirement of otologic surgery. To address this issue, the research group led by Weber has developed a system that employs a very accurate external tracking system with a small working volume positioned close to the target anatomy [9,10]. This system guides a robot that is mounted to the bed as near as possible to the patient and is used to drill a narrow path directly to the cochlea for a minimally invasive CI. Using this system, the group reports accuracies sufficient for otologic surgery.

The approach outlined in this paper uses a compact, bone-attached robot designed specifically for temporal bone milling. The direct fixation of the robot to the patient's skull eliminates the need for monitoring relative motion between the robot and the patient and permits highly accurate registration of the robot to the patient's anatomy. The compact robot design is suitable for the small surgical area of otologic procedures. Prior work using bone-attached robots has shown them to be capable of milling bone in orthopedic surgery [11–13] as well as providing effective alternatives to stereotactic frames for minimally invasive otologic surgery [14,15]. In this paper, we use a bone-attached robot to perform accurate mastoidectomies on cadaveric specimens. A preliminary description of the robot and some bench top tests, not including cadavers, appeared in Ref. [16].

2 Surgical Workflow

With the proposed robotic system, the workflow of the surgery involves pre-operative planning followed by a series of steps performed in the operating room (Fig. 2). Vital structures are segmented, i.e., identified, automatically in the pre-operative CT, including the facial nerve, chorda tympani, external auditory canal, semicircular canals, and ossicles using previously described methods [17,18]. Using the locations of these structures as guidance, the volume of bone to be removed in surgery is then manually segmented by the surgeon in the CT scan. In the operating room, a prepositioning frame (PPF), containing three titanium spheres, is attached to the patient using small screws via stab incisions. The spheres serve not only as fiducial markers for
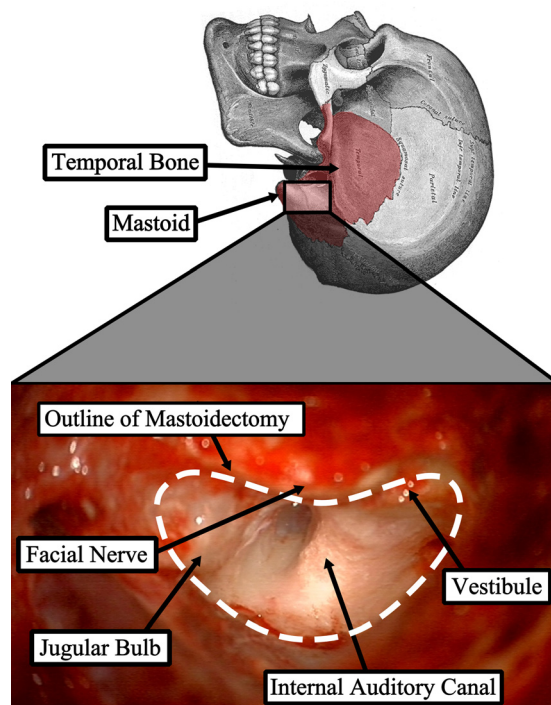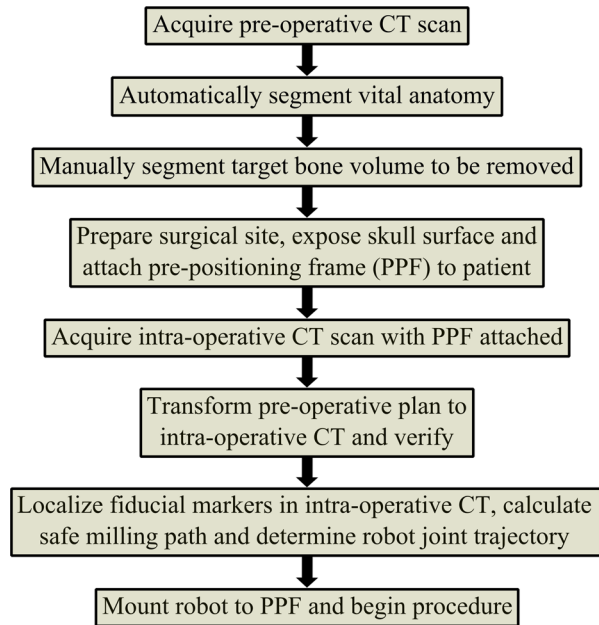

Fig. 1 Mastoid region of the temporal bone and photograph from surgical case showing the region after the target bone has been removed with several key anatomical structures identified

Fig. 2 Planning and workflow of surgical procedure

registering the robot to the patient's anatomy but also as attachment points for mounting the robot. An intra-operative CT scan of the patient with the PPF attached is then acquired. The CT is ideally performed in the operating room using either a portable CT scanner (e.g., xCAT ENT mobile CT scanner; Xoran Technologies, Ann Arbor, MI) or a fixed uni- or biplane rotational fluoroscopy machine. The intra-operative CT is registered to the pre-operative CT using intensity-based registration based on mutual information [19], and the pre-operative segmentations are transformed to the intra-operative CT using the registration. The robot is designed to attach to the spheres on the PPF in a known configuration. Localizing the spheres in the image [20] allows for the segmentation data to be transformed to the robot coordinate system using rigid registration based on sphere locations. The milling path is then calculated using a custom path planning algorithm and a robot trajectory is generated (described in Sec. 4).

The mastoidectomy begins with preparation of the surgical site by exposing the bone surface, after which the robot is attached to the PPF. The robot is then commanded to follow the planned trajectory to perform the bone milling. The procedure is monitored by the surgeon, who can adjust the speed of the robot, pause the robot, or stop the procedure at any time. Once the milling is complete, the robot is removed, and the surgeon performs any additional steps to complete the surgery.

3 Robotic System Overview

3.1 Design Considerations. Several experiments and data analyses were performed to identify design parameters and objectives for the robotic system. First, the forces while milling cortical bone (dense bone on the surface of the skull) as well as trabecular bone (pneumatized bone within the mastoid region) were measured to determine both the required range of forces that the robot must exert and the preferred cutting conditions. Formalin-fixed temporal bone specimens were milled with a surgical drill using an industrial robot under a variety of controlled cutting conditions. The forces were measured for the different cutting parameters, including different burr types, cutting angles, cutting velocities, and cutting depths. The details and full results of this study are presented in Ref. [21]; the key findings that affect robot design and trajectory planning are as follows:

(1) Large fluted burrs are preferred when anatomically possible to achieve lower forces for a given bone removal rate.

(2) Low shaft angles (i.e., cutting with the side of the burr) are desirable to minimize peak forces at the drill–bone interface.

(3) Shallow, high velocity cuts are better than slow, deep cuts to reduce average forces at the drill–bone interface.

(4) Pneumatized mastoid bone can be cut more aggressively than dense cortical bone.

Next, a workspace analysis was performed. Ten cadaveric temporal bone specimens with mastoidectomies performed by surgeons were used in this analysis. During mastoidectomy, the surgeons usually drill a wide region to facilitate easy identification of anatomy and avoid damage to vital structures. With the robot performing the procedure utilizing anatomic details from the pre-operative CT, it is possible to remove less bone while safely accessing the surgical targets. However, clinically relevant sized mastoidectomies were used in the analysis since they represent a conservative estimate of the required workspace dimensions.

A CT scan was acquired for each specimen, and the drilled volume of bone was segmented using a semi-automatic approach. The segmented drilled volumes (Fig. 3) of all specimens were aligned along their lateral surfaces. The Cartesian workspace volume that encompasses the drilled volumes of all specimens was determined to be approximately the shape of an inverted elliptical cone with maximum cross section on the lateral surface. The major and minor diameters of the ellipse on the lateral surface (similar to dashed outline in Fig. 3) were determined to be 52 mm and 45 mm, respectively, with the required depth being 41 mm.

The angular workspace required for mastoidectomy was also analyzed using the same set of specimens. If the target volume was convex relative to the lateral surface, a simple x–y–z stage would be sufficient to reach all of the target points. However, it has been observed through these specimens and actual surgical procedures that the surgical volume to drill might include a cavity to be drilled that is partially overhung with bone, requiring a tilting of the drill. The tilt requirements were evaluated by calculating the drill angle(s) required to safely reach each of the target points within the target volumes of the ten specimens (Fig. 3). It was determined that the surgery could be performed with a robot that has only one angular DOF with a range of motion of 50 deg
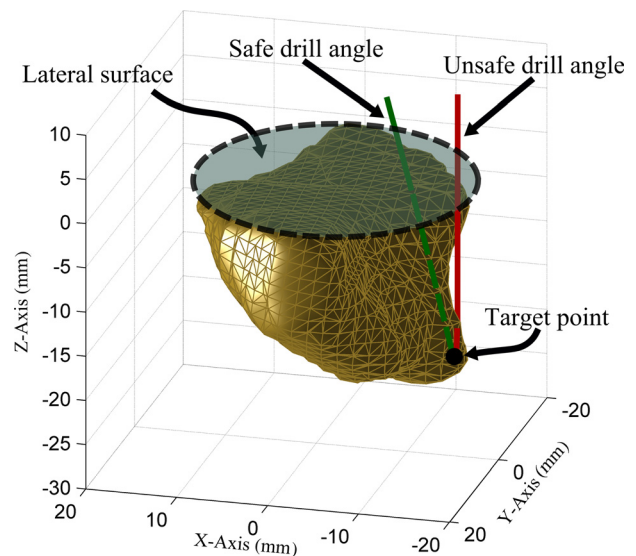

Fig. 3 Workspace analysis for the design of the robot. Drilled volume from one of the specimens is shown here with an example of safe and unsafe drill angles to reach a target location. At a safe drill angle, the shaft does not cross the boundary of the target volume except at the lateral surface. An unsafe drill angle causes the shaft to touch untargeted bone and/or other anatomy. The required angular workspace was calculated based on the range of angles needed to reach each point safely.
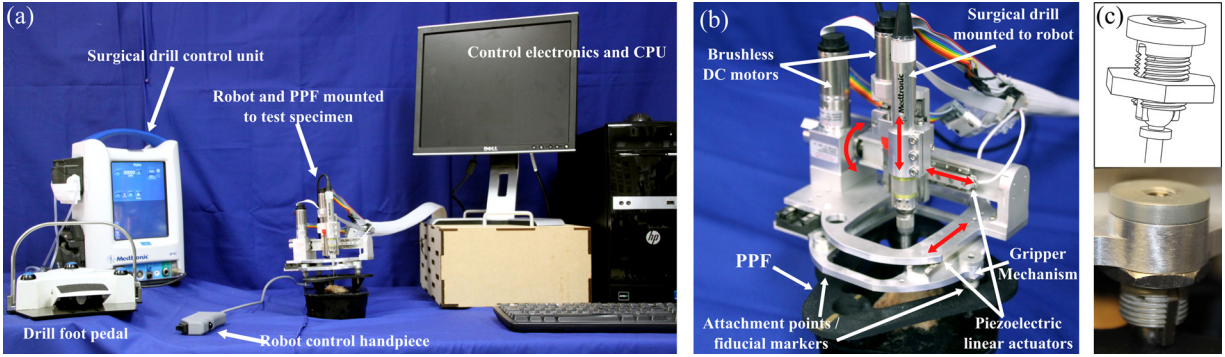
Fig. 4 (*a*) Surgical robotic system includes the robot that holds the surgical drill and mounts on the test specimen via the PPF, the surgical drill control unit and foot pedal for drill speed control, a control hand piece for adjusting robot motion and pausing/stopping the procedure, and the control electronics and computer/monitor, (*b*) close-up of the robot and PPF, and (*c*) Gripper mechanism used to attach robot to spheres on PPF

(4DOF total, including *x–y–z* motion). The robot must be aligned such that the single angular DOF aligns with the overhung area on the patient. The reduced complexity of the robot and limited sources of error associated with fewer joints (compared to a 6DOF robot) must be weighed against the additional requirement of aligning the robot with the patient anatomy. However, since the direction of the overhung region is consistent among patients, this alignment can be easily accomplished with a simple mechanism to show the surgeon the desired orientation to attach the robot.

3.2 Robot Prototype. Based on the above insights, we designed a 4DOF robot prototype with three translational joints and one rotational joint, analogous to a four-axis CNC milling machine (Fig. 4). Two different types of actuators are used: piezoelectric linear actuators (SmarAct GmbH, Oldenburg, Germany) and brushless DC motors (Maxon Precision Motor, Inc., Fall River, MA). The primary advantages of the piezoelectric actuators are their compact size and sterilizability. Initially, these actuators were planned for use in all joints; however, their limited blocking force when subjected to high frequency vibrations from the surgical drill did not permit them to be used for the two distal joints. Because of this limitation, a brushless motor and lead screw mechanism is used for the *z*-direction linear joint (the direction into the skull), and a brushless motor and antibacklash worm-wheel gearbox (Gysin AG, Itingen, Switzerland) is used for the rotational joint. A design goal for the final, clinical version of this device is for it to be completely sterilizable. The brushless motors used in this prototype are not sterilizable, but several manufacturers offer sterilizable versions (steam sterilization up to 273 °F) of similar size and power, which will be utilized in future versions.

The robot is fixed to the patient via the PPF (Fig. 4(*b*)), which is attached to the patient's skull using small screws. The robot mounts to the three spheres on the PPF with spherical gripper locking mechanisms (Fig. 4(*c*)). The drill spindle speed is controlled with a foot pedal and the robot motion is controlled with a small hand piece (Fig. 4(*a*)). This hand piece is used to adjust the speed of the robot, pause, or stop the procedure, if necessary.

4 Trajectory Planning

The path planning algorithm used in this study is an extension of an algorithm Danilchenko used in the earlier robotic mastoidectomy experiments with an industrial robot [7,22]. The input for this algorithm is a three-dimensional array of voxel elements such that each voxel's value serves as a label differentiating between air, targeted bone, forbidden bone, and the start/end point. The original algorithm finds a path for the drill's center that begins at the starting point, passes through every target voxel while avoiding all forbidden voxels and returns to the start/end point. Here,

we extend Danilchenko's algorithm in two important ways to model physical drill bit geometry. Danilchenko's algorithm assumes that the drill bit occupies only one cubic voxel and visits every voxel to be removed. However, a standard surgical bit is a sphere that covers many voxels.

First, to compensate for the size and shape of the bit, we use morphological operations. Figure 5(*a*) shows an example voxel input array for our path planning algorithm. While the actual arrays are three-dimensional, we show here a two-dimensional example to simplify the explanation. In the figure, R_1 (black) is the forbidden region and the union of regions R_2 (dark gray), R_3 (light gray), and R_4 (white) is the targeted voxel region input to our algorithm, which is intended to be removed with the drill bit if possible (it is the region the surgeon segmented that he/she desired the robot to remove). To ensure the preservation of the forbidden region, R_1, we modify the algorithm's input array using the morphological image processing operation known as dilation [23]. Dilation of a region expands its original boundary into its
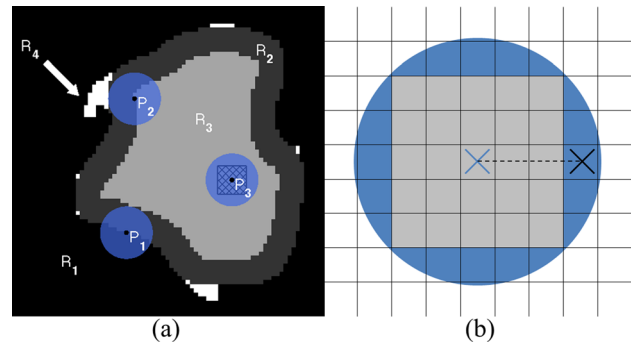

Fig. 5 (*a*) Illustration of the use of dilation to accommodate the finite size of the drill bit. Input targeted region is the combination of R_2, R_3, and R_4. Black is the forbidden region, R_1. Output targeted region, R_3, is light gray. The circular disk centered on P_1 represents the structuring element during preprocessing; the disk at P_2 represents the drill bit during ablation; and P_3 illustrates the super-voxel (hatched square). R_2 represents target voxels that will be removed by the edge of the drill. The white regions, R_4, are unreachable because of the bluntness of the bit. (*b*) Two-dimensional illustration of how the super-voxel approach improves the efficiency of the drilling process. The gray cells form the super-voxel within the drill bit (shaded circle) centered at the cross. When the drill bit is active at this location, all voxels within the super-voxel will be considered as hit and removed from the list of remaining target voxels. The next location for the center of the drill bit is the center of the nearest voxel outside the super-voxel, shown as the black cross. The cutting depth is the distance between the two crosses (length of the dashed line).

surroundings in a manner determined by the size and shape of a specified "structuring element." The structuring element used to dilate R_1 in our approach is the circle shown centered on P_1. The identical disk surrounding P_2 depicts the drill bit at a specific point on the output path. The dimensions of the structuring element are chosen to match those of the drill bit. The dilation of R_1 is accomplished by placing the center of the structuring element on every voxel in R_1 and moving all voxels within the structuring element into R_2. The new dilated forbidden region is the combination of R_1, R_2, and R_4.

The resultant modified targeted region, R_3, serves as input to the path planning algorithm, which determines a path for the center of the drill bit through a sequence of R_3 voxels such that all of the voxels in R_2 and R_3 are removed by some portion of the spherical drill tip. The drill's position, P_2, in the target region has been chosen to illustrate a limitation imposed by the bit's physical shape and size. Voxels in R_4 are located such that they cannot be removed by the drill bit without also removing at least one forbidden voxel. This problem is a consequence of the dimensions of the bit and also exists when the drilling is performed by hand. These unreachable nooks are filled in during the preprocessing dilation. Additionally, a check for connectedness ensures that we eliminate any isolated, unreachable pockets of R_3. All forbidden voxels are protected at the expense of allowing some targeted voxels to remain undrilled ensuring that the algorithm adheres to the rule "first do no harm." The drill angle associated with each target voxel is determined after the path is generated based on the location of the drill bit within the volume, the locations of nearby undrilled voxels, and potential collisions between the shaft and undrilled/untargeted bone.

Our second modification of Danilchenko's original algorithm stems from its requirement in that algorithm that the drill bit's center visit each target voxel, thereby leaving the relationship between the bit's physical size and the dimensions of the target voxels unexploited. We account for the size of the drill bit as it passes through the target voxel region, R_3, by creating a "super-voxel" centered on the drill bit and consisting of a group of target voxels whose size is determined by the desired cutting depth. As the path of the drill's center is planned through R_3, all of the target voxels within the super-voxel are considered to be removed (hatched square within P_3 shown in Fig. 5(a)). The identification of these voxels increases efficiency and results in considerable time savings. An exception to this rule occurs at those voxels in R_3 that border R_2. These voxels must be touched with the center of the drill bit to ensure that the entire original target region is removed. The super-voxel approach allows for the adjustment of the cutting depth of the drill bit by changing the number of target voxels contained within the super-voxel. For example, without the super-voxel approach, given a voxel size of $0.4 \times 0.4 \times 0.4$ mm, the commanded cutting depth of the drill would be 0.4 mm. Using the super-voxel approach, the cutting depth will be equal to the distance between the center of the super-voxel to the center of the nearest voxel outside the super-voxel (Fig. 5(b)). For example, given an image with voxel size of $0.4 \times 0.4 \times 0.4$ mm and a $5 \times 5 \times 5$ super-voxel, the cutting depth will be 1.2 mm.

5 Experimental Results

5.1 Free Space Accuracy Evaluation. The free space accuracy of the system was evaluated using the virtual target method described in Ref. [24] using a custom phantom and drill probe (Fig. 6). The robot attaches to the top of the phantom via three titanium spheres similar to how it would attach to the PPF. Seventeen titanium spheres are embedded on the bottom of the phantom to serve as validation markers to register the CT scan of the phantom to the coordinate measurement machine (CMM) used to test the accuracy in these experiments. The CMM used is a FARO GagePlus (FARO Technologies, Inc., Lake Mary, FL), which has an accuracy of 0.025 mm within its working volume. The CMM
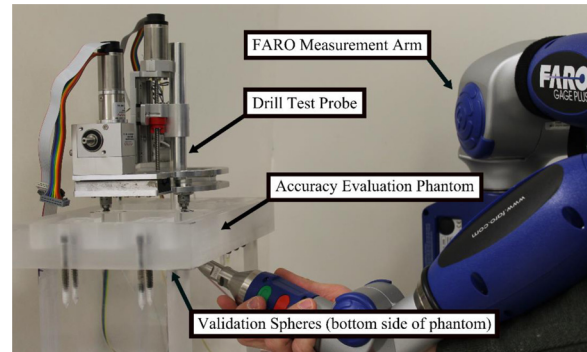

Fig. 6 Experimental setup for free space accuracy evaluation. The acrylic phantom contains attachment points for the robot on top and validation spheres for registering the experimental measurements to the CT target points on the bottom.

was used to localize the 17 validation spheres and measure the position of the drill probe at various positions. It was fixed to the same table as the phantom to minimize any relative motion.

Multiple scans of the phantom were taken using a portable CT scanner (xCAT ENT mobile scanner). Clinical CT scans of several patients were used to determine clinically relevant target points at which to test the accuracy of the system. Points on the bone surface, in regions close to the facial nerve, the vestibule, and the IAC were chosen as test points. These points were then superimposed onto the scan of the phantom to serve as the "virtual targets" in the experiment. Additionally, each of the 17 validation spheres and the three robot fiducial spheres were automatically localized in the CT scan of the phantom.

The robot was then mounted onto the test phantom, and the 17 validation spheres were localized using the CMM. The robot was programd to move the drill probe to the eight virtual target locations (defined in the CT scan and transformed to the robot space using the three fiducial sphere locations), and the probe tip was measured at each of these target points with the CMM. After the data were acquired, a rigid transformation with least-squares error was calculated between the CMM coordinate system and the CT image coordinate system using the validation spheres [25]. Then, the CMM measurements were transformed to the CT coordinate system and compared with the planned data points. The targeting error was then calculated. This error includes the various sources of error in the system, including both image processing/fiducial localization error as well as physical robot error. This procedure was repeated for three scans of the phantom and each scan used a different set of target points. The measurements for each set of points were repeated three times. The robot was removed from the phantom, powered down, re-attached, and run-through its full initialization process each time. The results of these experiments are summarized in Table 1. The mean and root mean square targeting error for all four regions were 0.50 mm or less.

5.2 Cadaver Experiments. Experiments in cadaveric temporal bones were then performed. The bones were formalin-fixed and previously frozen. Since the specimens used in these

Table 1 Error at various target regions in free space accuracy evaluation experiments

Location	RMS error (mm)	Mean error (mm)	Standard deviation (mm)
Skull surface	0.47	0.38	0.28
Facial nerve	0.49	0.42	0.26
Vestibule	0.50	0.43	0.26
I.A.C.	0.48	0.42	0.24

experiments are only partial temporal bones and the robot requires a larger surface area for attaching the PPF, the bones were cast in a hard urethane compound to provide enough space for the attachment. These experiments followed the surgical workflow outlined in Sec. 2 with one exception: the segmentations were performed in the scan acquired with the PPF attached (defined as intraoperative scan in Sec. 2) rather than the pre-operative scan before attaching the PPF. A 5 mm diameter spherical, fluted drill burr was used in all trials. After the procedure was completed, a postoperative CT scan was acquired. The removed volume was segmented using a semi-automatic method, and the postoperative scan was registered to the pre-operative scan for comparison of the planned versus milled volume and to check for violation of the critical anatomy. Additionally, the specimens were examined by an experienced surgeon postoperatively.

Mastoidectomies were performed on four temporal bone cadaveric specimens. A photograph of a bone after the experiment is shown in Fig. 7. The size of the segmented volumes ranged from 3.01 cm^3 to 8.85 cm^3. The error along the border of the target cavity was calculated by determining the distance between nearest border/surface points on the pre-operative and postoperative segmentations after the two scans were registered. The mean border error for all trials is 0.39 mm. The error for a test specimen is shown in Fig. 8. The border error results of the experiments are given in Table 2, along with the distances from the facial nerve and chorda tympani for each specimen. The first trial has higher
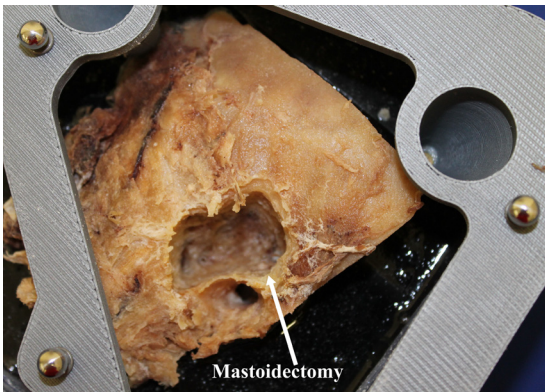
Table 2 Border error for the removed volume of bone and distances between the removed volume and vital anatomic structures for cadaver experiments

	Border error (mm)		Distance from vital nerves (mm)	
	Mean	Std.	Facial nerve	Chorda tympani
Bone 1	0.73	0.39	2.39	3.48
Bone 2	0.44	0.31	1.71	2.08
Bone 3	0.19	0.13	0.89	2.36
Bone 4	0.18	0.17	1.61	2.90

error margins along the surface. A prior version of the PPF was used for this first trial; however, this was replaced with a stiffer version for later trials, which reduced the error. Postoperative examination of all specimens revealed no damage to the vital anatomy.

6 Conclusions and Future Work

In this paper, we have described the design and testing of a bone-attached robotic system for mastoidectomy and a proposed surgical workflow of the system. The bone-attached approach reduces error in surgery by eliminating the need for an external tracking system. The attachment of the robot does require three additional small incisions; however, these are minor compared to the rest of the surgery and may be outweighed by the added benefit of having the robot fixed to the patient, which eliminates relative patient movement, fiducial marker occlusion, and robot/tracker calibration accuracy as potential sources of errors or failures. Similar incisions and frame fixation are required for stereotactic frames so the transition to attaching a robot for surgery is not expected to be a difficult adaptation for surgeons.

The experiments described in this paper target simple mastoidectomies. However, the system could be especially beneficial if used for surgeries that require additional bone removal, such as the translabyrinthine approach to remove acoustic neuromas. This surgery requires the removal of the labyrinth, which is in a dense bone located medial to the mastoid region and can take a significantly longer time to drill out because of its additional depth and the hardness of bone in this region.

Before this system can be clinically viable, several improvements must be made. The robot would fit into the current surgical workflow more smoothly if it were completely sterilizable. Then, the entire robot could be sterilized as a single piece prior to surgery, and there would be no need for bagging or for drapes between the robot and patient. The structural pieces of the robot as well as gears and other custom transmission components could be made with materials that can withstand steam sterilization temperatures. Currently, there are brushless DC motors on the market that are sterilizable (steam sterilization); however, they are designed for high-speed applications such as driving surgical drills, and there are currently no sterilizable motors with encoders. Therefore, these motors would have to be used with a large gear reduction and/or external rotary sensors to be effective for positioning tasks.

The next step in the experimental evaluation of this system is to perform experiments on complete cadaveric skulls and to use the full clinical workflow, including both the pre-operative and intraoperative CT scans. Additionally, the time of the procedure must be monitored and compared with the current method. Procedure time was not emphasized in these initial cadaver experimental trials; however, it is clear that improvements must be made to shorten the procedure time. A key factor in the success of a robotic surgical system, in addition to improving patient safety and allowing surgeons to perform procedures that they would not otherwise be able to perform, is cost. Much of the cost associated with surgery is operating room time. So, if the overall time of

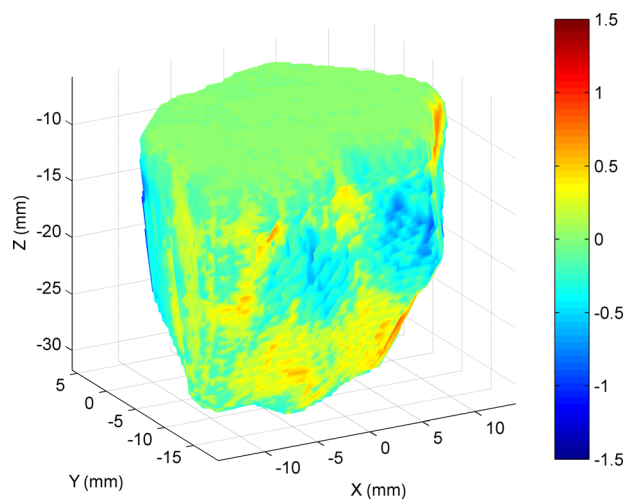**Fig. 7 Temporal bone specimen after robotic mastoidectomy**

Fig. 8 Surface error for a cadaver bone. The different colors along the surface represent the error between target and actual milled volumes. A negative error value indicates that the surface of the actual milled volume at that location was inside the planned volume.

procedure can be reduced to be at or below the current state of the art, a bone-attached robotic system for mastoidectomy may have the potential to be commercially successful.

Acknowledgment

References

[1] Paul, H. A., Bargar, W. L., Mittlestadt, B., Musits, B., Taylor, R. H., Kazanzides, P., Zuhars, J., Williamson, B., and Hanson, W., 1992, "Development of a Surgical Robot for Cementless Total Hip Arthroplasty," Clin. Orthop. Relat. Res., **285**, pp. 57–66.

[2] Glassman, E., Hanson, W. A., Kazanzides, P., Mittlestadt, B. D., Musits, B. L., Paul, H. A., and Taylor, R. H., 1992, "Image-Directed Robotic System for Precise Robotic Surgery Including Redundant Consistency Checking," U.S. Patent No. 5,086,401.

[3] Ho, S. C., Hibberd, R. D., and Davies, B. L., 1995, "Robot Assisted Knee Surgery," IEEE Eng. Med. Biol. Mag., **14**(3), pp. 292–300.

[4] Labadie, R. F., Majdani, O., and Fitzpatrick, J. M., 2007, "Image-Guided Technique in Neurotology," Otolaryngol. Clin. North Am., **40**(3), pp. 611–624.

[5] Federspil, P. A., Geisthoff, U. W., Henrich, D., and Plinkert, P. K., 2003, "Development of the First Force-Controlled Robot for Otoneurosurgery," Laryngoscope, **113**(3), pp. 465–471.

[6] Xia, T., Baird, C., Jallo, G., Hayes, K., Nakajima, N., Hata, N., and Kazanzides, P., 2008, "An Integrated System for Planning, Navigation and Robotic Assistance for Skull Base Surgery," Int. J. Med. Rob. Comput. Assisted Surg., **4**(4), pp. 321–330.

[7] Danilchenko, A., Balachandran, R., Toennies, J. L., Baron, S., Munske, B., Fitzpatrick, J. M., Withrow, T. J., Webster, R. J., and Labadie, R. F., 2011, "Robotic Mastoidectomy," Otol. Neurotol., **32**(1), pp. 11–16.

[8] Lim, H., Han, J.-M., Hong, J., Yi, B.-J., Lee, S. H., Jeong, J. H., Matsumoto, N., Oka, M., Komune, S., and Hashizume, M., 2011, "Image-Guided Robotic Mastoidectomy Using Human-Robot Collaboration Control," International Conference on Mechatronics and Automation (ICMA), Beijing, Aug. 7–10, pp. 549–554.

[9] Bell, B., Stieger, C., Gerber, N., Arnold, A., Nauer, C., Hamacher, V., Kompis, M., Nolte, L., Caversaccio, M., and Weber, S., 2012, "A Self-Developed and Constructed Robot for Minimally Invasive Cochlear Implantation," Acta Otolaryngol., **132**(4), pp. 355–360.

[10] Bell, B., Gerber, N., Williamson, T., Gavaghan, K., Wimmer, W., Caversaccio, M., and Weber, S., 2013, "In Vitro Accuracy Evaluation of Image-Guided Robot System for Direct Cochlear Access," Otol. Neurotol., **34**(7), pp. 1284–1290.

[11] Shoham, M., Burman, M., Zehavi, E., Joskowicz, L., Batkilin, E., and Kunicher, Y., 2003, "Bone-Mounted Miniature Robot for Surgical Procedures: Concept and Clinical Applications," IEEE Trans. Rob. Autom., **19**(5), pp. 893–901.

[12] Wolf, A., Jaramaz, B., Lisien, B., and DiGioia, A. M., 2005, "MBARS: Mini Bone-Attached Robotic System for Joint Arthroplasty," Int. J. Med. Rob. Comput. Assisted Surg., **1**(2), pp. 101–121.

[13] Plaskos, C., Cinquin, P., Lavallée, S., and Hodgson, A. J., 2005, "Praxiteles: A Miniature Bone-Mounted Robot for Minimal Access Total Knee Arthroplasty," Int. J. Med. Rob. Comput. Assisted Surg., **1**(4), pp. 67–79.

[14] Kratchman, L. B., Blachon, G. S., Withrow, T. J., Balachandran, R., Labadie, R. F., and Webster, R. J., 2011, "Design of a Bone-Attached Parallel Robot for Percutaneous Cochlear Implantation," IEEE Trans. Biomed. Eng., **58**(10), pp. 2904–2910.

[15] Kobler, J.-P., Kotlarski, J., Öltjen, J., Baron, S., and Ortmaier, T., 2012, "Design and Analysis of a Head-Mounted Parallel Kinematic Device for Skull Surgery," Int. J. Comput. Assisted Radiol. Surg., **7**(1), pp. 137–149.

[16] Dillon, N. P., Balachandran, R., dit Falisse, A. M., Wanna, G. B., Labadie, R. F., Withrow, T. J., Fitzpatrick, J. M., and Webster, R. J., 2014, "Preliminary Testing of a Compact Bone-Attached Robot for Otologic Surgery," Proc. SPIE, **9036**, p. 903614.

[17] Noble, J. H., Warren, F. M., Labadie, R. F., and Dawant, B. M., 2008, "Automatic Segmentation of the Facial Nerve and Chorda Tympani in CT Images Using Spatially Dependent Feature Values," Med. Phys., **35**(12), pp. 5375–5384.

[18] Noble, J. H., Dawant, B. M., Warren, F. M., and Labadie, R. F., 2009, "Automatic Identification and 3D Rendering of Temporal Bone Anatomy," Otol. Neurotol., **30**(4), pp. 436–442.

[19] Maes, F., Collignon, A., Vandermeulen, D., Marchal, G., and Suetens, P., 1997, "Multimodality Image Registration by Maximization of Mutual Information," IEEE Trans. Med. Imaging, **16**(2), pp. 187–198.

[20] Liu, X., Cevikalp, H., and Fitzpatrick, J. M., 2003, "Marker Orientation in Fiducial Registration," Proc. SPIE, **5032**, pp. 1176–1185.

[21] Dillon, N. P., Kratchman, L. B., Dietrich, M. S., Labadie, R. F., Webster, R. J., III, and Withrow, T. J., 2013, "An Experimental Evaluation of the Force Requirements for Robotic Mastoidectomy," Otol. Neurotol., **34**(7), pp. e93–e102.

[22] Danilchenko, A., 2011, "Fiducial-Based Registration With Anisotropic Localization Error," Ph.D. dissertation, Vanderbilt University, Nashville, TN.

[23] Sonka, M., Hlavac, V., and Boyle, R., 2014, *Image Processing, Analysis, and Machine Vision*, Cengage Learning, Stamford, CT.

[24] Balachandran, R., Mitchell, J. E., Dawant, B. M., and Fitzpatrick, J. M., 2009, "Accuracy Evaluation of MicroTargeting Platforms for Deep-Brain Stimulation Using Virtual Targets," IEEE Trans. Biomed. Eng., **56**(1), pp. 37–44.

[25] Fitzpatrick, J. M., and Sonka, M., 2000, *Handbook of Medical Imaging*: *Medical Image Processing and Analysis*, SPIE Press, Bellingham, WA.